Maximum likelihood tomographic reconstruction of extremely sparse solutions in diffuse fluorescence flow cytometry

Vivian Pera,* Eric Zettergren, Dana H. Brooks, and Mark Niedre

Department of Electrical and Computer Engineering, Northeastern University, Boston, Massachusetts 02115, USA
**Corresponding author: pera.v@husky.neu.edu*

Received April 18, 2013; accepted May 23, 2013;
posted June 4, 2013 (Doc. ID 189086); published June 28, 2013

We apply reparameterization and the maximum likelihood method to a specific fluorescence-mediated tomography problem where the solution is known *a priori* to be extremely sparse (i.e., all image values are zero except for one). Our algorithm performs significantly better than a standard image reconstruction method, particularly for deep-seated targets, and achieves close to 150 μm accuracy in a 3 mm diameter cross-sectional area with only 12 measurements. Moreover, results do not depend on the selection of a regularization parameter or other *ad hoc* values, and since reconstructions can be computed very quickly, the algorithm is also suitable for real-time implementation. © 2013 Optical Society of America

OCIS codes: (170.3010) Image reconstruction techniques; (110.6955) Tomographic imaging; (300.2530) Fluorescence, laser-induced.
http://dx.doi.org/10.1364/OL.38.002357

There are many areas of biomedical research where counting very rare circulating cells in small animals is important, such as studies of the immune system and early stage circulating tumor cells [1,2]. Fluorescence *in vivo* flow cytometry relies on microscopic interrogation of very small arterioles in the ear or retina of a mouse to noninvasively detect fluorescently labeled cells [3], but the sensitivity of this method is limited by the small blood volume sampled. Motivated by this, we recently developed a new technique termed diffuse fluorescence flow cytometry [4,5] that allows sampling of larger blood vessels with diffuse photons. In principle, the entire blood volume of a mouse can be interrogated in minutes, permitting detection of very rare labeled cell populations. We also demonstrated that we could coarsely localize labeled cells in the instrument field of view (FOV) using fluorescence-mediated tomography (FMT) [5]. Since both arteries and veins may be present in the FOV, localization is necessary to prevent cell overcounting, as the same cell may be redetected in a different blood vessel on the return trip through the vasculature. In practice, given our sampling rate, instrument FOV, and operating range (cell concentrations $<10^3$/mL), we expect only one cell in the FOV at a time. In this Letter, we show that we can leverage this sparsity to dramatically improve localization performance with low computational burden.

In recent years, regularizing inverse problems with an L1 norm has become a popular way of imposing a sparsity constraint [6,7]. Here we show that when the solution is known to be extremely sparse (i.e., all image values are zero except for one), an optimal approach is to reparameterize the problem and solve it with the maximum likelihood (ML) method. ML estimators are known to yield optimal performance in the limit of high signal-to-noise ratios (SNRs) and/or long data records [8], so they are often used to great advantage by the statistical signal processing community. In the field of diffuse optical imaging, this approach was employed in [9] for a case where the data was insensitive to target size, but the connection to sparsity was not made. We demonstrate that our algorithm performs significantly better than a standard FMT image reconstruction method, particularly for deep-seated targets, and achieves close to 150 μm accuracy in a 3 mm diameter cross-sectional area with only 12 measurements. Moreover, these results do not require the selection of a regularization parameter, and the algorithm is suitable for real-time applications.

A detailed description of the diffuse fluorescence flow cytometer (DFFC), along with analysis of *in vivo* data, has been previously reported in [4,5]. Briefly, the instrument consists of two 642 nm lasers that sequentially illuminate the sample from opposite sides [Fig. 1(a)]. The emitted fluorescent light is collected by six fiber optodes arranged in a ring around the sample and coupled to a high-sensitivity photon-counting photomultiplier tube array. The lasers are on–off modulated at a rate of 10 Hz to obtain 12 measurements (six measurements with each source) every 0.1 s, although the modulation rate could be increased for faster-moving cells. For the results presented here, we utilized a cylindrical cast polyester resin phantom with optical properties designed to match those of a mouse limb [4]. A picture of the 3 mm diameter phantom positioned in the center of the ring is displayed in Fig. 1(b). A strand of 250 μm (inner wall) diameter Tygon tubing, simulating a large blood vessel, was embedded in the phantom and is also visible. Flow cytometry calibration microspheres in a phosphate-buffered saline solution (which we showed previously to result in a negligible difference in signal strength compared to whole blood [10]) were pumped through the tube to mimic fluorescently labeled circulating cells.

As the microsphere travels through the instrument FOV, a transient "spike" is generated on all 12 channels [Fig. 1(c)], and it is the relative spike height differences across channels that allow us to localize the microsphere in the phantom cross section. Our previous results, obtained with a common FMT iterative image reconstruction algorithm, r-ART, demonstrated that we were able to successfully determine the angular position of

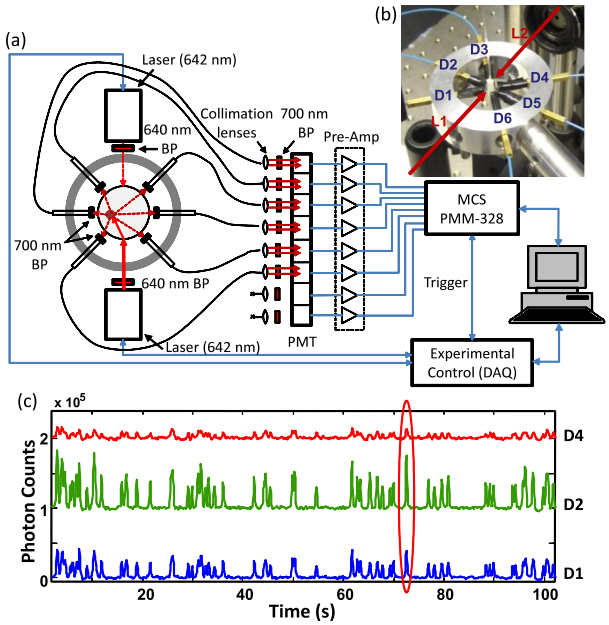

Fig. 1. (a) Schematic of DFFC with (b) photograph of detector ring and phantom in center; lasers and detectors labeled. (c) Sample data for microspheres (3 of 12 channels shown); one spike circled to highlight interchannel differences. The background was subtracted from each data set and an offset added for display purposes.

microspheres flowing through a shallowly embedded tube [Figs. 2(a) and 2(b)] [5]. When the tube was located deeper in the phantom, however, performance degraded significantly [Figs. 2(d) and 2(e)]. In our current approach, we assume that the signal from a microsphere or cell will occupy no more than one pixel. We are therefore interested in recovering the position of a point target, and it is by reparameterizing the problem in this manner that we can obtain an optimal ML solution without the use of a regularization parameter.

In the typical FMT problem, one seeks to recover a (vectorized) image $\boldsymbol{\eta}$ (e.g., fluorophore yield) defined by the linear system of equations $\mathbf{y} = \mathbf{W}\boldsymbol{\eta}$, where $\mathbf{W}$ is the sensitivity or weight matrix and $\mathbf{y}$ is the measurement vector. We computed $\mathbf{W}$ here by employing the diffusion approximation to the Boltzmann transport equation for an infinite homogeneous medium. Our photon-counting measurements have additive, channel-independent Poisson noise, but we have sufficient counts that we may approximate the Poisson distribution with a Gaussian. In the case of a point target, we can express $\boldsymbol{\eta}$ as the product of a scalar η and a unit vector $\mathbf{e}$, which contains zeros everywhere except for one component which is equal to 1. Our data model is therefore

$$\mathbf{y} \sim \mathcal{N}(\eta \mathbf{W}\mathbf{e}(\mathbf{r}), \mathbf{R}), \tag{1}$$

where the location of the nonzero component of $\mathbf{e}$ depends on the position of the point target $\mathbf{r}$, and $\mathbf{R}$ is a diagonal covariance matrix containing the mean of the measurements on its diagonal (i.e., $[\mathbf{R}]_{jj} = [\eta \mathbf{W}\mathbf{e}(\mathbf{r})]_j$). We estimated the components of $\mathbf{R}$ by using the mean of the background signal in a 10 s window centered on each measurement, since even our tallest spikes are usually only ~5% of the background level. The ML estimates of η and $\mathbf{r}$ are obtained by maximizing Eq. (1) with respect to these variables, which yields

$$\hat{\eta}(\mathbf{r}) = \frac{\mathbf{e}(\mathbf{r})^T \mathbf{W}^T \mathbf{R}^{-1} \mathbf{y}}{\mathbf{e}(\mathbf{r})^T \mathbf{W}^T \mathbf{R}^{-1} \mathbf{W}\mathbf{e}(\mathbf{r})}, \tag{2}$$

$$\hat{\mathbf{r}} = \underset{\mathbf{r}}{\operatorname{argmax}} \frac{|\mathbf{e}(\mathbf{r})^T \mathbf{W}^T \mathbf{R}^{-1} \mathbf{y}|^2}{\mathbf{e}(\mathbf{r})^T \mathbf{W}^T \mathbf{R}^{-1} \mathbf{W}\mathbf{e}(\mathbf{r})}, \tag{3}$$

where we have let $\eta = \hat{\eta}(\mathbf{r})$ in Eq. (3) to eliminate the dependency on η. We note that in the case of Gaussian noise, the ML approach reduces to a weighted least squares estimate of η and $\mathbf{r}$. In other words, to determine the position of a cell, the ML method takes each column of the sensitivity matrix, scales it appropriately, and correlates it with the data. The one that best matches the data maximizes Eq. (3) and indicates the location of the cell.

We plotted Eq. (3) as a function of $\mathbf{r}$ for two different measured data vectors in Figs. 2(c) and 2(f). As shown, the resulting surfaces are smooth with a single peak. The location of the peak, indicated by a blue dot, corresponds well with the location of the tube in Figs. 2(a) and 2(d), respectively. We performed simulations at various SNRs to determine the accuracy with which the position of the peak may be ascertained. Although the details of that analysis are beyond the scope of this Letter, we have determined that in the instrument's operating SNR range, easily including the microsphere data reported here, the ML estimate of the position of the peak is unbiased and the precision is better than 50 μm. In theory, we can therefore obtain excellent accuracy with this approach, although in practice performance is affected by unmodeled sources of error, such as (mouse) movement artifacts, interchannel calibration, and data-forward model mismatch. Generating this surface and determining the position of the peak on a 50 μm grid (dimension of $\mathbf{W}$ is 12×2817) takes ~0.02 s with nonoptimized Matlab code on a laptop, so this algorithm is suitable for real-time implementation.

We used our algorithm to determine the position of microspheres flowing through a tube embedded in a phantom at various orientations and depths. Each 0.1 s

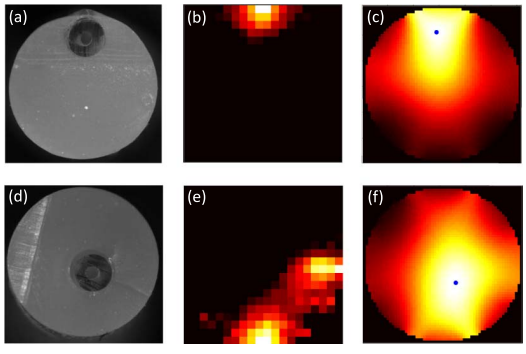

Fig. 2. (a) Photograph of phantom cross section with shallow tube. (b) Previous r-ART result. (c) ML surface; dot indicates position of peak. (d)–(f) Same as (a)–(c) but for deep tube.

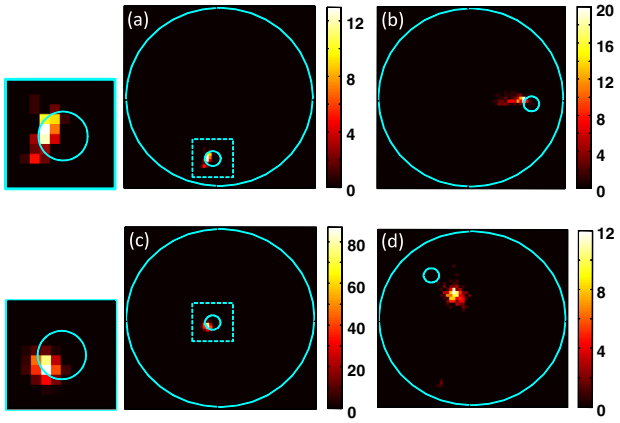

Fig. 3. (a)–(d) Two-dimensional histograms of microsphere positions obtained with ML method; left insets show close-ups for (a) and (c). Circumference of phantom and the inner wall of tube is overlayed in light blue.

time bin was processed independently, meaning that each position determination was based on only 12 measurements. Typical results from four of seven experiments are displayed in Figs. 3(a)–3(d), which show two-dimensional histograms of microsphere positions, with each pixel color-coded according to how many times the algorithm selected that pixel as the location of the microsphere. A total of ~1200 microsphere position estimates were analyzed.

In general, localization performance was very good. The results were tightly clustered, possessing a spread (i.e., standard deviation) of ~100 μm, well within the 250 μm inner diameter of the Tygon tube. Performance for the deeply embedded tube [Fig. 3(c)] is comparable to that observed in the shallow cases, in contrast to [5], where performance was significantly worse at greater depths. In most instances, the centers of the reconstructed clusters in the histograms were within 3 pixels (150 μm) of the center of the tube. The larger bias observed in Fig. 3(d) occurs in a minority of cases and is most likely caused by phantom positioning errors.

In this initial implementation, we made a number of simplifications that may have adversely impacted algorithm performance. For example, the sensitivity matrix employed was based on the diffusion equation approximation, which is known to be problematic in the case of small path lengths on the order of 3 mm. Additional bias may have also resulted from coregistration errors between the white light cross-sectional images, which were used to determine the location of the tube, and the DFFC data sets. We expect performance to improve with a Monte Carlo-derived sensitivity matrix that more accurately models the instrument and sample geometry and a better coregistration procedure.

In conclusion, we have demonstrated that in cases where the point-target model applies, an effective way of imposing a sparsity constraint is to reparameterize the problem and solve it with the ML method. Examples of other situations that might justify a point-target model include the detection of early stage tumors or micrometastases in bulk tissue [11] and cases where the data is insensitive to target size [9]. Our approach leads to an algorithm that delivers significantly improved localization performance, especially in the case of deeply embedded targets. The algorithm is also quick and therefore amenable to real-time implementation. Furthermore, performance does not depend on the selection of a regularization parameter.

In the future, we hope to extend this approach to the case where more than one cell is present in the FOV. Preliminary modeling suggests that if anatomical prior information is available, we can accommodate 2–3 cells present in the FOV simultaneously and still maintain close to real-time performance. We also plan to incorporate the time history of our detections to improve specificity.

We thank Stacey Markovic and Tushar Swamy for their help with instrumentation and data collection. This work was funded by grants (5R21HL098750) and (R01EB012117) from the National Institutes of Health.

References

1. C. Lo Celso, H. E. Fleming, J. W. Wu, C. X. Zhao, S. Miake-Lye, J. Fujisaki, D. Cote, D. W. Rowe, C. P. Lin, and D. T. Scadden, Nature **457**, 92 (2009).
2. J. B. Smerage and D. F. Hayes, Cancer Invest. **26**, 109 (2008).
3. J. Novak, I. Georgakoudi, X. Wei, A. Prossin, and C. P. Lin, Opt. Lett. **29**, 77 (2004).
4. E. Zettergren, D. Vickers, J. M. Runnels, S. K. Murthy, C. P. Lin, and M. Niedre, J. Biomed. Opt. **17**, 037001 (2012).
5. E. Zettergren, T. Swamy, J. Runnels, C. P. Lin, and M. Niedre, Phys. Med. Biol. **57**, 4627 (2012).
6. P. Mohajerani, A. A. Eftekhar, J. Huang, and A. Adibi, Appl. Opt. **46**, 1679 (2007).
7. J. Dutta, S. Ahn, C. Li, S. R. Cherry, and R. M. Leahy, Phys. Med. Biol. **57**, 1459 (2012).
8. S. M. Kay, *Fundamentals of Statistical Signal Processing: Estimation Theory* (Prentice-Hall, 1993).
9. A. B. Milstein, M. D. Kennedy, P. S. Low, C. A. Bouman, and K. J. Webb, Appl. Opt. **44**, 2300 (2005).
10. E. Zettergren, D. Vickers, J. Runnels, C. P. Lin, and M. J. Niedre, *Proceedings of the IEEE Engineering in Medicine and Biololgy Society, 2011 Annual International Conference of the IEEE* (IEEE, 2011), p. 486.
11. D. C. Comsa, T. J. Farrell, and M. S. Patterson, Phys. Med. Biol. **51**, 3733 (2006).